Research Square

Preprints are preliminary reports that have not undergone peer review.
They should not be considered conclusive, used to inform clinical practice,
or referenced by the media as validated information.

Ultra-low loss piezo-optomechanical low-confinement silicon nitride platform for visible wavelength quantum photonic circuits

Mayank Mishra

mayank1@arizona.edu

University of Arizona

Gwangho Choi

University of Arizona

Wenhua He

University of Arizona

Gina Talcott

Sandia National Laboratories

Katherine Kearney

Sandia National Laboratories

Michael Gehl

Sandia National Laboratories https://orcid.org/0000-0002-2967-8507

Andrew Leenheer

Sandia National Laboratories https://orcid.org/0000-0003-4735-292X

Daniel Dominguez

Sandia National Laboratories

Nils Otterstrom

Sandia National Laboratories

Matt Eichenfield

University of Arizona https://orcid.org/0000-0003-0863-7877

Article

Keywords:

Posted Date: March 12th, 2026

DOI: https://doi.org/10.21203/rs.3.rs-8962716/v1

License: This work is licensed under a Creative Commons Attribution 4.0 International License.
Read Full License

Additional Declarations: There is **NO** Competing Interest.

Ultra-low loss piezo-optomechanical low-confinement silicon nitride platform for visible wavelength quantum photonic circuits

Mayank Mishra[1], Gwangho Choi[1], Wenhua He[1], Gina M. Talcott[2], Katherine Kearney[2], Michael Gehl[2], Andrew Leenheer[2], Daniel Dominguez[2], Nils T. Otterstrom[2*], Matt Eichenfield[1,2,3*]

[1*]James C. Wyant College of Optical Sciences, University of Arizona, Tucson, Arizona, 85721, USA.
[2]Microsystems Engineering, Science, and Applications, Sandia National Laboratories, Albuquerque, New Mexico, 87185, USA.
[3]Electrical, Computer and Energy Engineering, University of Colorado, Boulder, Colorado, 80309, USA.

*Corresponding author(s). E-mail(s): ntotter@sandia.gov; Matt.Eichenfield@colorado.edu;

Abstract

The stringent demands of photonic quantum computing protocols motivate photonic integrated circuit (PIC) platforms with passive optical properties such as extremely low losses and correspondingly large circuit depths, as well as active optical properties such as high reconfiguration rates, low power dissipation, and minimal crosstalk. At the same time, many quantum photonic resource state generators, such as single-photon sources and quantum memories, require operation in the visible wavelength range. These requirements make the passive optical properties of CMOS-fabricated, ultralow-loss, low-confinement silicon nitride waveguides especially attractive. However, the conventional active properties of these systems based on thermo-optic modulation are plagued by high levels of crosstalk, slow modulation rates, and high power dissipation. Although there have been recent demonstrations of CMOS-fabricated, visible wavelength, piezo-optomechanical PICs that solve the above challenges associated with implementing active functionality, these have made use of high-confinement waveguides with currently demonstrated losses of order **0.3–1 dB/cm**, precluding circuit depths required for scalable quantum algorithms. Here, we demonstrate that combining piezo-optomechanical actuation with a low-confinement, ultra-low loss

silicon nitride platform addresses the scalability challenge while enabling high-performance active functionality at visible wavelengths. This platform achieves a propagation loss **0.026 dB/cm** at **780 nm**, modulation bandwidths in the MHz range, and a phase shifter voltage-length product ($\boldsymbol{V_\pi L}$) of approximately **2.8 V · m** and negligible hysteresis. We further demonstrate reconfigurable Mach-Zehnder interferometers based on spiral phase shifters with 0.63 dB loss per phase shifter.

Introduction

Recent work in high-confinement, piezo-optomechanical photonic integrated circuits (PICs) in the visible wavelength regime has demonstrated high circuit densities, fast modulation rates, and low power dissipation/consumption [1–6]. Given this set of capabilities, piezo-optomechanical PICs could be well-suited for visible wavelength scalable quantum photonic information processing applications such as integrated quantum resource state generators [7], linear optical computing [8], hybrid spin-photon quantum computing architectures [6], quantum networking protocols [9], and quantum sensors [10]. However, the propagation losses in these high-confinement waveguides remain, in many cases, too high to achieve the circuit depths and low error rates necessary for scalable quantum computing [11]. In contrast, low-confinement silicon nitride (Si_3N_4) waveguides, which feature high-aspect ratio silicon nitride cores and extremely thick silicon dioxide claddings, have the potential to address this scaling challenge by offering ultra-low propagation losses [12, 13]. These waveguides have shown exceptionally low optical losses of less than 0.1 dB/m [14, 15] at telecommunication wavelengths and below 1 dB/m [16, 17] at visible wavelengths. These low-confinement waveguide platforms deliver high optical power-handling capabilities and a wide transparency window [18, 19]. Furthermore, they support the realization of ultra-high-Q resonators [20] and provide a pathway for integration with quantum systems, including rubidium atoms [21], strontium atoms [22], and InAs quantum dots [23].

The integration of thermo-optic modulators [20, 24, 25] and PZT-based piezo-optomechanical actuators [26–28] with low-confinement silicon nitride waveguides has been demonstrated, but both approaches exhibit significant limitations. Thermo-optic modulators typically exhibit slow modulation speeds, high power consumption/dissipation, and large crosstalk. On the other hand, PZT-based devices offer higher modulation speed and lower crosstalk but suffer from significant ferroelectric hysteresis and integration limitations due to CMOS-incompatibility. In contrast, piezo-optomechanical actuator platforms based on aluminum nitride (AlN) implemented using CMOS foundry processes offer a promising alternative [1–3, 5, 29]. Although so far only demonstrated with high-confinement waveguides, these AlN actuators provide high modulation bandwidths (exceeding 100 MHz), ultralow power consumption with negligible hysteresis, and compatibility with cryogenic operation.

The much thicker silicon dioxide claddings required by low-confinement silicon nitride waveguides present a key challenge for piezo-optomechanical actuation and strain-optic phase shifters. Without careful design, the increased oxide thickness leads

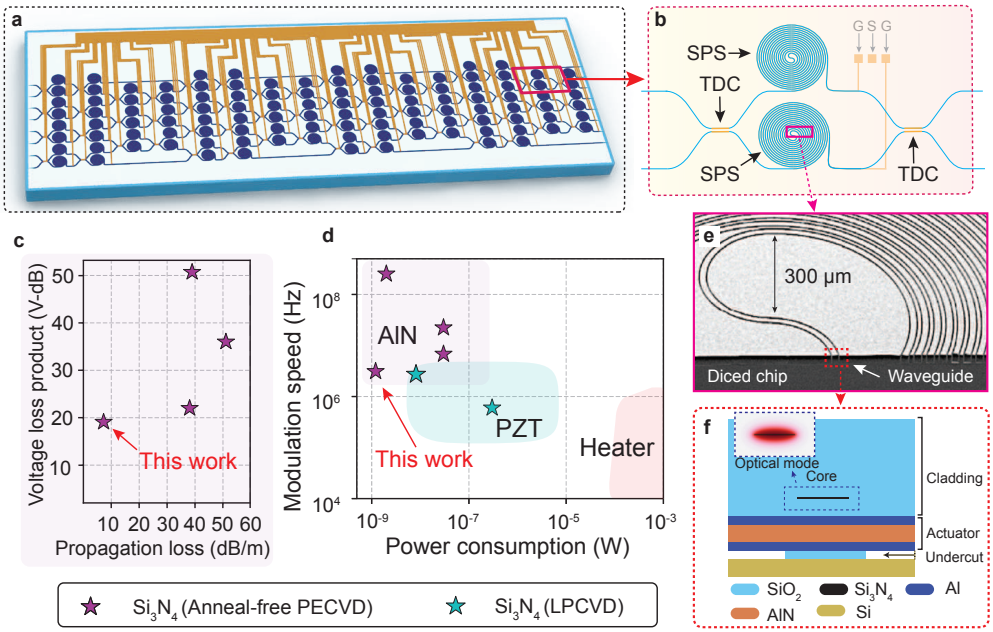


Fig. 1 Low-confinement silicon nitride piezo-optomechanical platform. **(a)** Schematic representation of the eight-mode linear programmable nanophotonic processor (LPNP) circuit, based on the Clements et al. [30] architecture, featuring a network of Mach-Zehnder interferometers (MZIs) and phase shifters. **(b)** Schematic of an MZI incorporating two Archimedean spiral phase shifters (SPSs) and two tunable directional couplers (TDCs). **(c)** Comparison of the voltage-loss product (VLP) and propagation loss across existing visible wavelength aluminum nitride-based piezo-optomechanical modulator platforms [1, 2]. **(d)** Comparison of modulation speed and power consumption for visible wavelength silicon nitride (Si_3N_4) based modulator platforms [1, 2, 24, 26, 28]. The Si_3N_4 platforms include devices fabricated via low-pressure chemical vapor deposition (LPCVD) and anneal-free plasma-enhanced chemical vapor deposition (PECVD). Details on the loss and VLP values for existing visible wavelength Si_3N_4 platforms are provided in Supplementary Table 1. **(e)** Scanning electron microscope (SEM) image showing the cross-section of a wafer diced through the center of an on-chip SPS, with a minimum bending radius of 150 μm at the center. **(f)** Cross-sectional schematic of a low-confinement waveguide-based piezo-optomechanical phase modulator, highlighting the different material layers. Inset: x-component of the electric field of the fundamental optical mode in a low-confinement waveguide, simulated using the finite element method.

to high mechanical rigidity and, consequently, reduced piezo-optomechanical responsivity. In this work, we show that thick silicon dioxide claddings with an extended undercut beneath the actuator can enable geometries and aspect ratios that concentrate the distribution of stress and optical field within the core and cladding of the waveguide in a way that allows high piezo-optomechanical responsivity even with thick claddings. Moreover, because a large fraction of the optical field in these low-confinement waveguides resides in the silicon dioxide cladding, the comparatively stronger photoelastic response of silicon dioxide [29, 31], despite its lower refractive index than silicon nitride, compensates for the reduced mechanical compliance (see Supplementary Fig. 3d and Supplementary Fig. 3e). Experimentally,

we demonstrate a design achieving piezo-optomechanical responsivity comparable to high-confinement systems while lowering optical loss by an order of magnitude [1]. In the following sections, we present the device performance and loss characterization of our low-confinement platform, and show, through an example, how reduced loss leads to orders-of-magnitude improvements in the success probability of heralding multi-photon quantum states in LPNP circuits.

Results

Low-confinement waveguide platform

The fundamental programmable element of low-confinement waveguide linear programmable nanophotonic processor (LPNP) platform (Fig. 1a) is a Mach-Zehnder interferometer (MZI; Fig. 1b) with integrated output phase shifters. These MZIs utilize Archimedean-spiral-shaped waveguide phase shifters to reduce both the device footprint and optical bending losses. A scanning electron micrograph of a spiral phase-shifter (SPS) section fabricated using an anneal-free plasma-enhanced chemical vapor deposition (PECVD) process [1, 2, 5, 32] is shown in Fig. 1e. Compared to conventional low-pressure chemical vapor deposition (LPCVD), the anneal-free PECVD approach enables low-temperature processing, allowing seamless monolithic integration with CMOS metal routing for the actuator beneath the waveguide, which would otherwise be damaged by high-temperature annealing. As detailed in subsequent sections and highlighted in Fig. 1c, our low-confinement waveguides establish a new benchmark in voltage-loss product (VLP) and propagation loss among visible wavelength, anneal-free PECVD-fabricated silicon nitride waveguides with AlN piezo-optomechanical actuators. Additionally, as shown in Fig. 1d, these devices achieve high modulation speeds in the MHz range and exhibit low holding power in the nanowatt range ($P_{\text{hold}} < 1$ nW for a 5 V applied voltage at room temperature), comparable to other visible wavelength modulators employing AlN-based piezo-optomechanical strain actuator platforms [1, 2].

Fig. 1f illustrates the integration of the low-confinement waveguide with a piezo-optomechanical actuator. A scanning electron micrograph of the waveguide is shown in Fig. 2a, with the thin core highlighted in yellow (false color). The fabricated waveguide features a 50 nm-thick, 3.6 μm-wide core, positioned 2.96 μm above the actuator, and is embedded within a SiO_2 cladding that is 12.5 μm-thick and 15.8 μm-wide at the core height, as depicted in Fig. 2a. The actuator, shown in Fig. 2b, consists of a 0.46 μm-thick aluminum nitride layer sandwiched between two 0.25 μm-thick aluminum electrodes, connected to electrical signals through ground-signal-ground (GSG) contact pads. To characterize the SPS, we integrate it into one arm of an imbalanced MZI, as illustrated in Fig. 2c. Adiabatic tapers (2 mm long) at both input and output ports gradually widen the core from 0.4 μm to 3.6 μm, ensuring fundamental mode excitation [33] and minimizing coupling loss.

When a voltage difference ΔV is applied across the electrical contacts, it generates a vertical electric field given by $E_3 \approx \Delta V / t_{\text{AlN}}$, where t_{AlN} is the AlN layer thickness. This electric field induces strain in the structure, described by the strain

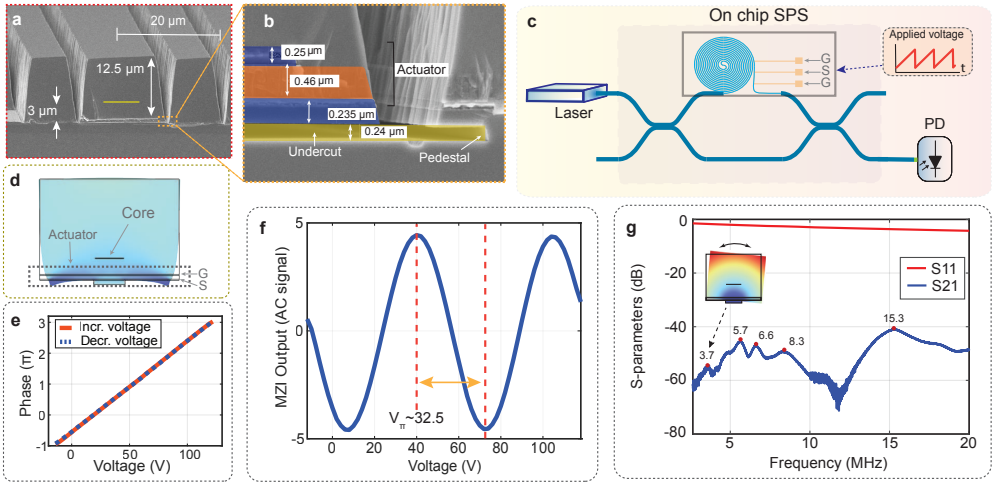


Fig. 2 Piezo-optomechanical phase shifter characterization.
(a, b) Cross-sectional SEM images of the fabricated phase modulators. In **(b)**, blue and orange false colors highlight the electrode and the AlN actuator layer, respectively, which is suspended by an undercut. **(c)** Schematic of the imbalanced MZI used for characterization, incorporating an on-chip spiral phase shifter in one arm, two off-chip 50:50 beam splitters, a 780 nm laser, and a photodetector. A ramp voltage (red) is applied to the piezo-optomechanical actuator, modulating the phase and producing a sinusoidal optical output. **(d)** Schematic cross-section of the phase shifter with FEM-simulated s_{11} strain distribution and the corresponding (exaggerated) waveguide deformation for clarity. **(e)** Measured phase response of the MZI for increasing and decreasing voltage sweeps from -10 V to 120 V and back, showing negligible hysteresis. **(f)** Measured optical response of the MZI under a 200 Hz ramp voltage applied to the piezo-optomechanical SPS. An 8.7 cm SPS achieves a π phase shift at 32.5 V. **(g)** Measured S-parameter spectra (S11, S21) of the SPS, showing strong S21 resonances at 3.7, 5.7, 6.6, and 8.3 MHz and negligible S11 response over 0–20 MHz. Inset: simulated mechanical eigenmode at 3.7 MHz.

tensor s_{kl}, with the s_{11} component illustrated in Fig. 2d. The induced strain modulates the effective refractive index (n_{eff}) of the waveguide via two primary mechanisms: the photoelastic effect ($\Delta n_{\mathrm{eff,PE}}$) and the moving boundary effect ($\Delta n_{\mathrm{eff,MB}}$) [5, 29]. The relative change of refractive index under strain is conventionally described by the strain-optic coefficient as $\Delta(1/n^2)_{\mathrm{ij}} = \sum_{\mathrm{k,l}} p_{\mathrm{ijkl}} s_{\mathrm{kl}}$, where p_{ijkl} is the photoelastic tensor [29, 31, 34]. The strain components are related to the applied electric field by $s_{\mathrm{kl}} = \sum_{\mathrm{m}} d_{\mathrm{mkl}} E_{\mathrm{m}}$, where d_{mkl} represents the piezoelectric coupling tensor. The total change in effective refractive index per applied volt, $\Delta n_{\mathrm{eff}} = \Delta n_{\mathrm{eff,PE}} + \Delta n_{\mathrm{eff,MB}}$, produces a phase shift in the optical mode given by $\Delta\phi = \frac{2\pi}{\lambda} \Delta n_{\mathrm{eff}} L$. Using two-dimensional finite element method (FEM) simulations of the waveguide cross section (as shown in Fig. 2d and the inset of Fig. 1f), we calculate the voltage-length product ($V_\pi L$):

$$V_\pi L = \frac{\lambda}{2} \left(\frac{\Delta n_{\mathrm{eff}}}{\Delta V} \right)^{-1}, \tag{1}$$

where $\Delta n_{\mathrm{eff}}/\Delta V$ is the change in the effective refractive index per applied volt. Supplementary Fig. 6 and Fig. 7 further analyze how $V_\pi L$ varies with geometry.

To characterize the modulator, we apply a 200 Hz ramp signal to the SPS, sweeping the voltage from −10 V to 120 V. The resulting optical response exhibits sinusoidal fringes due to the MZI transfer function, with negligible hysteresis between the forward and reverse voltage sweeps, as shown in Fig. 2e. From these measurements, we extract an average V_π of approximately 32.5 V. For the 8.7-cm-long spiral phase shifter at $\lambda =$ 780 nm, this corresponds to a voltage-length product of $V_\pi L = 2.8$ V $\cdot$ m. Additional measurement details on other tested devices are provided in Supplementary Fig. 4.

These devices are tested well below any mechanical resonance frequencies. Although operating at or above resonance can enhance the optomechanical response, it also induces narrowband behavior, ringing, and phase lag, so the fundamental eigenfrequency ultimately sets the upper limit of the usable bandwidth. We characterized the mechanical resonance frequencies using a vector network analyzer (VNA), as shown in Fig. 2G. The transmission coefficient S_{21} exhibits prominent resonance peaks at 3.7 MHz (fundamental), 5.7 MHz, 6.6 MHz, and 8.3 MHz, while the reflection coefficient S_{11} shows negligible response over the 0–20 MHz range. From the observed fundamental eigenfrequency of 3.7 MHz, we estimate the pedestal width of our devices using FEM simulations to be approximately 1.4 μm. Using this geometry in the simulations, together with the experimentally measured $V_\pi L = 2.8$ V $\cdot$ m and reported literature values for $|p_{12}|$ and $|p_{44}|$ [29], we evaluate the possible values of the silicon nitride photoelastic coefficients. Because $p_{44} = (p_{11} - p_{12})/2$, there are four candidate combinations of p_{11} and p_{12}, and only $p_{11} = -0.125$ and $p_{12} = 0.047$ yield simulated values of $V_\pi L$ consistent with the experimental measurement of 2.8 V $\cdot$ m. These findings indicate that silicon dioxide dominates the strain-induced effective refractive index change, whereas silicon nitride contributes an opposing effect, as discussed in Supplementary Note 1 and Note 2.

Loss characterization of low-confinement waveguide

The overall attenuation (α) of optical modes in low-confinement waveguides arises from both intrinsic material properties and device geometry. Advances in fabrication have substantially reduced material absorption losses [35], making geometry-dependent losses the primary contributors to total attenuation. These losses include (i) actuator absorption, (ii) scattering from interfacial roughness, (iii) radiation from waveguide bends, (iv) mode coupling loss at the fiber-to-waveguide interface, and (v) crosstalk between adjacent waveguides. Among these, absorption and scattering losses are particularly sensitive to waveguide dimensions (see Supplementary Note 6 and Supplementary Fig. 7), as variations in core and cladding size can significantly alter modal overlap with absorptive or rough regions. We combine FEM simulations with analytical loss models to estimate the propagation loss in our low-confinement platform, as described in Supplementary Note 7 and illustrated in Supplementary Fig. 7 and Fig. 8. Using the estimated photoelastic constants, we identify an optimal waveguide geometry by minimizing the voltage–loss product, as discussed in Supplementary Note 6 and Note 8 and summarized in Supplementary Fig. 8.

We characterized the propagation loss using a top-down imaging technique (Ref. [36], Fig. 3a) in two distinct low-confinement waveguide geometries: (i) an unetched waveguide without an actuator (Fig. 3c) and (ii) an etched waveguide with

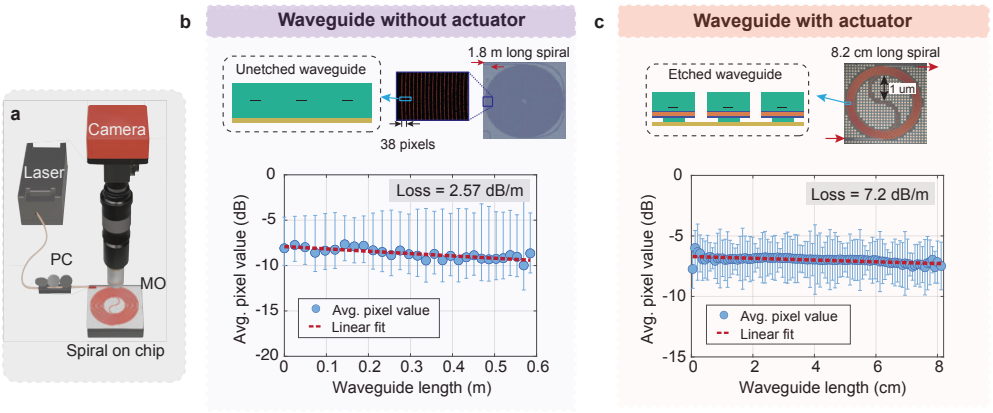


Fig. 3 Waveguide-loss measurement using top-view imaging.
(a) Schematic of the experimental setup for measuring waveguide loss using a top-down micrograph technique. The setup includes a 780 nm laser, polarization controller (PC), and a camera equipped with a 12× zoom lens and a 5× microscope objective (MO). **(b)** Propagation loss characterization of an unetched 1.8 m silicon nitride Archimedean spiral waveguide (no actuator). Image analysis of a spiral section shows the average pixel intensity versus propagation distance; linear fitting yields a loss of 2.57 dB/m. **(c)** Propagation loss analysis of an etched 8.2 cm-long Archimedean spiral waveguide with an integrated bottom actuator. Image processing of the complete spiral structure and pixel-intensity averaging along its length yield a propagation loss of 7.2 dB/m.

a bottom actuator (Fig. 3d). In the unetched device, the dominant loss mechanism is scattering at the core–cladding interface due to fabrication imperfections. By contrast, the etched waveguide with an integrated actuator exhibits additional losses from actuator absorption as well as scattering at both the core–cladding and cladding–air interfaces. The top-down imaging technique (Fig. 3a) collects light scattered perpendicular to the direction of optical mode propagation. This method is based on the principle that the local intensity of scattered light is directly proportional to the remaining guided power within the waveguide. For the unetched waveguide shown in Fig. 3c, we image a section of the 1.8-m-long Archimedean spiral, where adjacent waveguides in the image are separated by approximately 38 pixels, corresponding to 2.4 cm of waveguide length along the spiral. We apply a 20-pixel-wide analysis window following the waveguide curvature to calculate the average pixel intensity for each waveguide segment. By plotting these intensity values against the propagation length of the optical mode along the spiral and performing a linear fit, we extract a propagation loss of 2.57 dB/m.

For the etched waveguide with actuator shown in Fig. 3d, we image the entire 8.2-cm-long spiral in a single field of view and average pixel intensities along its length. We divide the spiral into 100 sections and each 0.82-mm-long section corresponds to a data point in the Fig. 3d plot. In each section, we apply a 15-pixel averaging window that covers the waveguide. Linear fitting of these data points yields a propagation loss of 7.2 dB/m, approximately 2.8 higher than in the unetched case. We cross-validate these results using optical time-domain reflectometry (OTDR) with a femtosecond laser, which yields a propagation loss of 6.1 dB/m for the actuator-free waveguide,

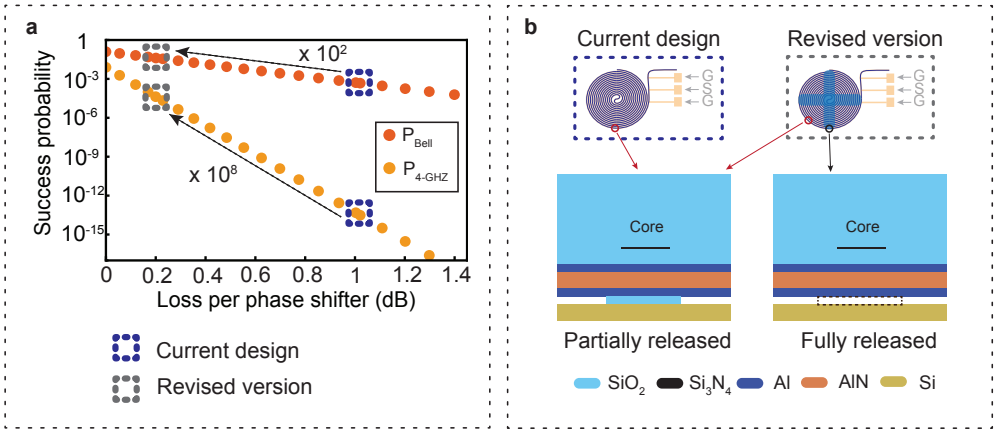


Fig. 4 Simulated performance scaling and proposed SPS geometry.
(a) Success probability for generating heralded Bell states and 4-mode GHZ states within a lossy LPNP circuit. The arrows highlight the significant improvement in success probability achieved by reducing the loss per phase shifter from 1 dB/m to 0.2 dB/m; this reduction yields probability enhancement factors of $\sim 10^2$ for Bell states and $\sim 10^8$ for 4-mode GHZ states (see Supplementary Note 4 for details). **(b)** Schematic of two SPS designs: the presently demonstrated device (partially released) and a proposed revised version (with fully released sections). The revised design aims to minimize the propagation loss per phase shifter in the LPNP circuit toward the low-loss regime (0.2 dB/m) simulated in **(a)**.

while direct transmission measurements provide a propagation loss of 3.8 dB/m and an insertion loss of 1.9 dB per facet. These complementary techniques show reasonable agreement with the imaging-based results and confirm that propagation losses remain below 10 dB/m across all measurement methods. Detailed analysis procedures, noise correction methods, and measurement protocols are provided in Supplementary Note 5 and Supplementary Fig. 6.

Discussion

Using a top-down propagation loss measurement approach, we measure propagation losses of 7.2 dB/m with an actuator and 2.57 dB/m without an actuator for our low-confinement waveguides fabricated via the PECVD process. The higher loss in waveguides with actuators is attributed to additional modal absorption by the top metal electrodes. We employ these waveguides as phase shifters with a length of 8.7 cm and propagation loss of 0.626 dB, achieving a voltage–length product of approximately 2.8 V $\cdot$ m at 780 nm, corresponding to a VLP of about 20.16 V $\cdot$ dB. In comparison, state-of-the-art high-confinement platforms using the same strain-induced change in effective refractive index report VLP values of approximately 50.7 V $\cdot$ dB [1] with propagation losses of $35 - 100$ dB/m. Another high-confinement platform that relies on strain-induced optical path length modulation achieves a VLP of 22 V $\cdot$ dB [2]. Our low-confinement platform can leverage this same optical path length modulation

mechanism by fully releasing selected SPS sections to further reduce VLP (see Supplementary Fig. 1a and Fig. 1b). As shown in Supplementary Fig. 1a, this approach could reduce $V_\pi L$ of the low-confinement platform by a factor of $5-10\times$ relative to current devices, potentially lowering the VLP to ~ 4 V $\cdot$ dB or below.

We estimate the impact of reduced loss in LPNP circuits through an example protocol for the on-demand generation of heralded Bell and GHZ states using a four-mode and eight-mode linear programmable nanophotonic processor [7, 30, 37]. For this analysis, we consider propagation loss in the phase shifters as the sole loss mechanism, assuming all other components are lossless. The loss per phase shifter, γ, is equal to the ratio of VLP to the maximum applied voltage (V_{max}). At $V_{max} = 20$ V, our low-confinement waveguide platform (VLP ~ 20 V $\cdot$ dB) incurs a loss of ~ 1 dB per phase shifter, whereas a future low-confinement platform (shown in Fig. 4b and Supplementary Fig. 1) with $V_\pi L < 3$ V $\cdot$ m (VLP < 4 V $\cdot$ dB) would suffer a loss of < 0.2 dB per phase shifter. Fig. 4a illustrates how this difference translates into the probability of successfully heralding quantum states in a lossy LPNP circuit with ideal detectors. The results indicate dramatic improvements in quantum-state generation efficiency: for Bell-state preparation in a four-mode LPNP circuit, the success probability increases by roughly two orders of magnitude for the lower phase-shifter loss, and for heralded four-mode GHZ states, the success probability improves by a factor of $\sim 10^8$. Details of the calculation supporting these results are provided in Supplementary Note 4 and Supplementary Fig. 5.

This low-loss, scalable architecture forms the essential hardware backbone for applications such as quantum routers [9], universal quantum photonic logic circuits [38, 39], on-chip quantum memories for heralded entanglement swapping [40], tunable low-power optical true-time delay lines [41], and post-selected heralded GHZ state generation [7, 37]. Furthermore, the platform's ultra-low propagation loss and anneal-free, foundry-compatible fabrication process enable seamless integration of single-photon sources, modulators, and electronic control, paving the way for complex, scalable, and fully integrated quantum photonic systems on a single chip.

Materials and methods

Devices measurement

To characterize the devices, we drive the SPS using a Keysight 33500B function generator as a voltage source in combination with a Thorlabs BPA100 benchtop high-voltage piezo amplifier, which provides a noise bandwidth from 20 Hz to 100 kHz. We apply a 200 Hz ramp modulation signal to the SPS (Fig. 2c), sweeping the voltage up to 120 V. We perform S-parameter measurements using a Keysight P9374A vector network analyzer. We measure the holding power with a Keithley 2450 source-measure unit, as shown in Supplementary Fig. 4b.

Top-down imaging measurement

Fig. 3a shows the experimental setup used to measure waveguide loss with a top-down imaging technique. We capture images using an Allied Vision 1800 U-120c camera

(1280 × 960 pixels) equipped with a Navitar 12× UltraZoom Video Microscopy System and a Mitutoyo 5× microscope objective (MO). Because the low-confinement waveguides exhibit extremely low loss and therefore weak light scattering, we adjust the imaging parameters during acquisition to improve the signal-to-noise ratio. For the unetched waveguide, where we image a section of the 1.8 m-long spiral, we use a gamma correction of 0.5, a gain of 35 dB, and an exposure time of 8.03 ms. For the etched waveguide with an actuator, we set the gamma correction to 0.5, the gain to 38.3 dB, and the exposure time to 7.3 ms.

Acknowledgments

This material is based upon work supported by the U.S. Department of Energy, Office of Science, National Quantum Information Science Research Centers, Quantum Systems Accelerator.

Author contributions:

N.T.O. and M.E. conceived the work. M.M. wrote the manuscript. M.M., G.C., W.H., G.M.T., K.K., M.G., A.L., D.D., N.T.O., and M.E. contributed to the experiments, simulations, and data analysis. M.M., G.C., G.M.T., N.T.O and M.E. contributed to the revision of the paper. All authors discussed the results and implications.

Competing interests:

The authors declare that they have no competing interests.

Data and materials availability:

The data and code that support the findings of this study are available from the corresponding author upon reasonable request. All data needed to evaluate the conclusions in the paper are present in the paper and/or the Supplementary Materials. Additional data related to this paper may be requested from the authors.

References

[1] Dong, M., Clark, G., Leenheer, A.J., Zimmermann, M., Dominguez, D., Menssen, A.J., Heim, D., Gilbert, G., Englund, D., Eichenfield, M.: High-speed programmable photonic circuits in a cryogenically compatible, visible–near-infrared 200 mm cmos architecture. Nature Photonics **16**(1), 59–65 (2022) https://doi.org/10.1038/s41566-021-00903-x

[2] Dong, M., Heim, D., Witte, A., Clark, G., Leenheer, A.J., Dominguez, D., Zimmermann, M., Wen, Y.H., Gilbert, G., Englund, D., Eichenfield, M.: Piezo-optomechanical cantilever modulators for VLSI visible photonics. APL Photonics **7**(5), 051304 (2022) https://doi.org/10.1063/5.0088424

[3] Dong, M., Zimmermann, M., Heim, D., Choi, H., Clark, G., Leenheer, A.J., Palm, K.J., Witte, A., Dominguez, D., Gilbert, G., Eichenfield, M., Englund, D.: Programmable photonic integrated meshes for modular generation of optical entanglement links. npj Quantum Information **9**(1), 42 (2023) https://doi.org/10.1038/s41534-023-00708-6

[4] Palm, K.J., Dong, M., Golter, D.A., Clark, G., Zimmermann, M., Chen, K.C., Li, L., Menssen, A., Leenheer, A.J., Dominguez, D., Gilbert, G., Eichenfield, M., Englund, D.: Modular chip-integrated photonic control of artificial atoms in diamond waveguides. Optica **10**(5), 634–641 (2023) https://doi.org/10.1364/OPTICA.486361

[5] Stanfield, P.R., Leenheer, A.J., Michael, C.P., Sims, R., Eichenfield, M.: Cmos-compatible, piezo-optomechanically tunable photonics for visible wavelengths and cryogenic temperatures. Opt. Express **27**(20), 28588–28605 (2019) https://doi.org/10.1364/OE.27.028588

[6] Clark, G., Raniwala, H., Koppa, M., Chen, K., Leenheer, A., Zimmermann, M., Dong, M., Li, L., Wen, Y.H., Dominguez, D., Trusheim, M., Gilbert, G., Eichenfield, M., Englund, D.: Nanoelectromechanical control of spin–photon interfaces in a hybrid quantum system on chip. Nano Letters **24**(4), 1316–1323 (2024) https://doi.org/10.1021/acs.nanolett.3c04301 https://doi.org/10.1021/acs.nanolett.3c04301. PMID: 38227973

[7] Bhatti, D., Barz, S.: Generating greenberger-horne-zeilinger states using multi-port splitters. Physical Review A **107**(3), 033714 (2023)

[8] Kazanskiy, N.L., Butt, M.A., Khonina, S.N.: Optical computing: Status and perspectives. Nanomaterials **12**(13) (2022) https://doi.org/10.3390/nano12132171

[9] Lee, Y., Bersin, E., Dahlberg, A., Wehner, S., Englund, D.: A quantum router architecture for high-fidelity entanglement flows in quantum networks. npj Quantum Information **8**(1), 75 (2022) https://doi.org/10.1038/s41534-022-00582-8

[10] Ibrahim, M.I., Foy, C., Kim, D., Englund, D.R., Han, R.: Room-temperature quantum sensing in cmos: On-chip detection of electronic spin states in diamond color centers for magnetometry. In: 2018 IEEE Symposium on VLSI Circuits, pp. 249–250 (2018). https://doi.org/10.1109/VLSIC.2018.8502329

[11] Rudolph, T.: Why i am optimistic about the silicon-photonic route to quantum computing. APL photonics **2**(3) (2017)

[12] Bauters, J.F., Heck, M.J.R., John, D., Dai, D., Tien, M.-C., Barton, J.S., Leinse, A., Heideman, R.G., Blumenthal, D.J., Bowers, J.E.: Ultra-low-loss high-aspect-ratio si3n4 waveguides. Opt. Express **19**(4), 3163–3174 (2011) https://doi.org/10.1364/OE.19.003163

[13] Hong, S., Zhang, L., Wang, Y., Zhang, M., Xie, Y., Dai, D.: Ultralow-loss compact silicon photonic waveguide spirals and delay lines. Photon. Res. **10**(1), 1–7 (2022) https://doi.org/10.1364/PRJ.437726

[14] Bauters, J.F., Heck, M.J.R., John, D.D., Barton, J.S., Bruinink, C.M., Leinse, A., Heideman, R.G., Blumenthal, D.J., Bowers, J.E.: Planar waveguides with less than 0.1 db/m propagation loss fabricated with wafer bonding. Opt. Express **19**(24), 24090–24101 (2011) https://doi.org/10.1364/OE.19.024090

[15] Jin, W., Yang, Q.-F., Chang, L., Shen, B., Wang, H., Leal, M.A., Wu, L., Gao, M., Feshali, A., Paniccia, M., Vahala, K.J., Bowers, J.E.: Hertz-linewidth semiconductor lasers using cmos-ready ultra-high-q microresonators. Nature Photonics **15**(5), 346–353 (2021) https://doi.org/10.1038/s41566-021-00761-7

[16] Chauhan, N., Isichenko, A., Wang, J., Blumenthal, D.J.: Sub-db/m loss integrated 103 and 90 million q resonators for laser stabilization at rubidium and strontium wavelengths. In: 2022 IEEE Photonics Conference (IPC), pp. 1–2 (2022). https://doi.org/10.1109/IPC53466.2022.9975529

[17] Chauhan, N., Wang, J., Bose, D., Liu, K., Compton, R.L., Fertig, C., Hoyt, C.W., Blumenthal, D.J.: Ultra-low loss visible light waveguides for integrated atomic, molecular, and quantum photonics. Opt. Express **30**(5), 6960–6969 (2022) https://doi.org/10.1364/OE.448938

[18] Blumenthal, D.J.: Photonic integration for UV to IR applications. APL Photonics **5**(2), 020903 (2020) https://doi.org/10.1063/1.5131683

[19] Blumenthal, D.J., Heideman, R., Geuzebroek, D., Leinse, A., Roeloffzen, C.: Silicon nitride in silicon photonics. Proceedings of the IEEE **106**(12), 2209–2231 (2018) https://doi.org/10.1109/JPROC.2018.2861576

[20] Isichenko, A., Hunter, A.S., Bose, D., Chauhan, N., Song, M., Liu, K., Harrington, M.W., Blumenthal, D.J.: Sub-hz fundamental, sub-khz integral linewidth self-injection locked 780 nm hybrid integrated laser. Scientific Reports **14**(1), 27015 (2024) https://doi.org/10.1038/s41598-024-76699-x

[21] Isichenko, A., Chauhan, N., Bose, D., Wang, J., Kunz, P.D., Blumenthal, D.J.: Photonic integrated beam delivery for a rubidium 3d magneto-optical trap. Nature Communications **14**(1), 3080 (2023) https://doi.org/10.1038/s41467-023-38818-6

[22] Chauhan, N., Isichenko, A., Liu, K., Wang, J., Zhao, Q., Behunin, R.O., Rakich, P.T., Jayich, A.M., Fertig, C., Hoyt, C.W., Blumenthal, D.J.: Visible light photonic integrated brillouin laser. Nature Communications **12**(1), 4685 (2021) https://doi.org/10.1038/s41467-021-24926-8

[23] Chanana, A., Larocque, H., Moreira, R., Carolan, J., Guha, B., Melo, E.G.,

Anant, V., Song, J., Englund, D., Blumenthal, D.J., Srinivasan, K., Davanco, M.: Ultra-low loss quantum photonic circuits integrated with single quantum emitters. Nature Communications **13**(1), 7693 (2022) https://doi.org/10.1038/s41467-022-35332-z

[24] Yong, Z., Chen, H., Luo, X., Govdeli, A., Chua, H., Azadeh, S.S., Stalmashonak, A., Lo, G.-Q., Poon, J.K.S., Sacher, W.D.: Power-efficient silicon nitride thermo-optic phase shifters for visible light. Opt. Express **30**(5), 7225–7237 (2022) https://doi.org/10.1364/OE.448614

[25] Liu, K., Chauhan, N., Song, M., Harrington, M.W., Nelson, K.D., Blumenthal, D.J.: Tunable broadband two-point-coupled ultra-high-q visible and near-infrared photonic integrated resonators. Photon. Res. **12**(9), 1890–1898 (2024) https://doi.org/10.1364/PRJ.528398

[26] Hosseini, N., Dekker, R., Hoekman, M., Dekkers, M., Bos, J., Leinse, A., Heideman, R.: Stress-optic modulator in triplex platform using a piezoelectric lead zirconate titanate (pzt) thin film. Opt. Express **23**(11), 14018–14026 (2015) https://doi.org/10.1364/OE.23.014018

[27] Wang, J., Liu, K., Harrington, M.W., Rudy, R.Q., Blumenthal, D.J.: Silicon nitride stress-optic microresonator modulator for optical control applications. Opt. Express **30**(18), 31816–31827 (2022) https://doi.org/10.1364/OE.467721

[28] Montifiore, N., Isichenko, A., Chauhan, N., Wang, J., Hunter, A.S., Harrington, M.W., Chawlani, R., Rudy, R.Q., Kierzewski, I., Pushkarsky, M., Blumenthal, D.J.: Blue to Near-IR Integrated PZT Silicon Nitride Modulators for Quantum and Atomic Applications (2026). https://arxiv.org/abs/2601.15695

[29] Tian, H., Liu, J., Attanasio, A., Siddharth, A., Blésin, T., Wang, R.N., Voloshin, A., Lihachev, G., Riemensberger, J., Kenning, S.E., Tian, Y., Chang, T.H., Bancora, A., Snigirev, V., Shadymov, V., Kippenberg, T.J., Bhave, S.A.: Piezoelectric actuation for integrated photonics. Adv. Opt. Photon. **16**(4), 749–867 (2024) https://doi.org/10.1364/AOP.529288

[30] Clements, W.R., Humphreys, P.C., Metcalf, B.J., Kolthammer, W.S., Walmsley, I.A.: Optimal design for universal multiport interferometers. Optica **3**(12), 1460–1465 (2016) https://doi.org/10.1364/OPTICA.3.001460

[31] Gyger, F., Liu, J., Yang, F., He, J., Raja, A.S., Wang, R.N., Bhave, S.A., Kippenberg, T.J., Thévenaz, L.: Observation of stimulated brillouin scattering in silicon nitride integrated waveguides. Phys. Rev. Lett. **124**, 013902 (2020) https://doi.org/10.1103/PhysRevLett.124.013902

[32] Dong, M., Boyle, J.M., Palm, K.J., Zimmermann, M., Witte, A., Leenheer, A.J., Dominguez, D., Gilbert, G., Eichenfield, M., Englund, D.: Synchronous micromechanically resonant programmable photonic circuits. Nature Communications

14(1), 7716 (2023) https://doi.org/10.1038/s41467-023-42866-3

[33] Chiu, C., Liao, Y.-H.: The critical adiabatic linear tapered waveguide combined with a multimode waveguide coupler on an soi chip. International Journal of Optics **2019**(1), 4270612 (2019)

[34] Dixon, R.W.: Photoelastic Properties of Selected Materials and Their Relevance for Applications to Acoustic Light Modulators and Scanners. Journal of Applied Physics **38**(13), 5149–5153 (1967) https://doi.org/10.1063/1.1709293

[35] Corato-Zanarella, M., Ji, X., Mohanty, A., Lipson, M.: Absorption and scattering limits of silicon nitride integrated photonics in the visible spectrum. Opt. Express **32**(4), 5718–5728 (2024) https://doi.org/10.1364/OE.505892

[36] Jaber, N., Madaras, S., Starbuck, A., Pomerene, A., Dallo, C., Trotter, D.C., Gehl, M., Otterstrom, N.: Non-resonant bragg scattering four-wave mixing at near-visible wavelengths in low-confinement silicon nitride waveguides. Opt. Lett. **49**(11), 3146–3149 (2024) https://doi.org/10.1364/OL.519793

[37] Bhatti, D., Barz, S.: Heralding higher-dimensional bell and greenberger–horne–zeilinger states using multiport splitters. New Journal of Physics **27**(3), 033006 (2025)

[38] Taballione, C., Meer, R., Snijders, H.J., Hooijschuur, P., Epping, J.P., Goede, M., Kassenberg, B., Venderbosch, P., Toebes, C., Vlekkert, H., Pinkse, P.W.H., Renema, J.J.: A universal fully reconfigurable 12-mode quantum photonic processor. Materials for Quantum Technology **1**(3), 035002 (2021) https://doi.org/10.1088/2633-4356/ac168c

[39] Carolan, J., Harrold, C., Sparrow, C., Martín-López, E., Russell, N.J., Silverstone, J.W., Shadbolt, P.J., Matsuda, N., Oguma, M., Itoh, M., Marshall, G.D., Thompson, M.G., Matthews, J.C.F., Hashimoto, T., O'Brien, J.L., Laing, A.: Universal linear optics. Science **349**(6249), 711–716 (2015) https://doi.org/10.1126/science.aab3642

[40] Dhara, P., Englund, D., Guha, S.: Entangling quantum memories via heralded photonic bell measurement. Phys. Rev. Res. **5**, 033149 (2023) https://doi.org/10.1103/PhysRevResearch.5.033149

[41] Ji, X., Yao, X., Gan, Y., Mohanty, A., Tadayon, M.A., Hendon, C.P., Lipson, M.: On-chip tunable photonic delay line. APL Photonics **4**(9), 090803 (2019) https://doi.org/10.1063/1.5111164

Supplementary Files

This is a list of supplementary files associated with this preprint. Click to download.

- Supplementaryinformation.pdf